Cardiac C-arm computed tomography using a 3D + time ROI reconstruction method with spatial and temporal regularization

Cyril Mory[a)]
Université de Lyon, CREATIS; CNRS UMR5220; Inserm U1044; INSA-Lyon; Université Lyon 1, F-69621 Villeurbanne Cedex, France; and Philips Research Medisys, 33 rue de Verdun, 92156 Suresnes, France

Vincent Auvray and Bo Zhang
Philips Research Medisys, 33 rue de Verdun, 92156 Suresnes, France

Michael Grass and Dirk Schäfer
Philips Research, Röntgenstrasse 24–26, D-22335 Hamburg, Germany

S. James Chen and John D. Carroll
Department of Medicine, Division of Cardiology, University of Colorado Denver, 12605 East 16th Avenue, Aurora, Colorado 80045

Simon Rit
Université de Lyon, CREATIS; CNRS UMR5220; Inserm U1044; INSA-Lyon; Université Lyon 1; and Centre Léon Bérard, 28 rue Laënnec, F-69373 Lyon, France

Françoise Peyrin
Université de Lyon, CREATIS; CNRS UMR5220; Inserm U1044; INSA-Lyon; Université Lyon 1, F-69621 Villeurbanne Cedex, France; and X-ray Imaging Group, European Synchrotron, Radiation Facility, BP 220, F-38043 Grenoble Cedex, France

Philippe Douek and Loïc Boussel
Université de Lyon, CREATIS; CNRS UMR5220; Inserm U1044; INSA-Lyon; Université Lyon 1; and Hospices Civils de Lyon, 28 Avenue du Doyen Jean Lépine, 69500 Bron, France

Purpose: Reconstruction of the beating heart in 3D + time in the catheter laboratory using only the available C-arm system would improve diagnosis, guidance, device sizing, and outcome control for intracardiac interventions, e.g., electrophysiology, valvular disease treatment, structural or congenital heart disease. To obtain such a reconstruction, the patient's electrocardiogram (ECG) must be recorded during the acquisition and used in the reconstruction. In this paper, the authors present a 4D reconstruction method aiming to reconstruct the heart from a single sweep 10 s acquisition.
Methods: The authors introduce the 4D RecOnstructiOn using Spatial and TEmporal Regularization (short 4D ROOSTER) method, which reconstructs all cardiac phases at once, as a 3D + time volume. The algorithm alternates between a reconstruction step based on conjugate gradient and four regularization steps: enforcing positivity, averaging along time outside a motion mask that contains the heart and vessels, 3D spatial total variation minimization, and 1D temporal total variation minimization.
Results: 4D ROOSTER recovers the different temporal representations of a moving Shepp and Logan phantom, and outperforms both ECG-gated simultaneous algebraic reconstruction technique and prior image constrained compressed sensing on a clinical case. It generates 3D + time reconstructions with sharp edges which can be used, for example, to estimate the patient's left ventricular ejection fraction.
Conclusions: 4D ROOSTER can be applied for human cardiac C-arm CT, and potentially in other dynamic tomography areas. It can easily be adapted to other problems as regularization is decoupled from projection and back projection. © *2014 American Association of Physicists in Medicine*. [http://dx.doi.org/10.1118/1.4860215]

Key words: C-arm, computed tomography, heart, ROOSTER, compressed sensing

1. INTRODUCTION

Reconstruction of the beating heart in 3D + time in the catheter laboratory using only the available C-arm system would improve diagnosis, guidance, device sizing, and outcome control for intracardiac interventions, e.g., electrophysiology,[1] valvular disease treatment,[2] structural or congenital heart disease. However, the design of a suitable acquisition protocol and of the corresponding 3D + time reconstruction method is still a challenging problem. A high resolution and almost artifact-free 3D reconstruction can be obtained by performing an ungated Feldkamp (FDK) reconstruction,[3] but the resulting volume is static and moving organs are blurred. The goal is to reconstruct a 3D + time sequence of volumes in which the motion is rendered accurately. For the acquisition part, the C-arm rotates around the patient while acquiring projections and recording the patient's electrocardiogram. The length of the acquisition, the number

of projections to be acquired, and whether the C-arm should perform a single or multiple sweeps are still open questions, since there is no standard protocol for cardiac C-arm imaging today. Optimized cardiac C-arm computed tomography (cardiac C-arm CT) acquisition protocols for cardiac imaging prior to transcatheter aortic valve implantation (TAVI) have been presented.[2,4] The parameters to optimize include rotation speed, number of rotations, number of projections, electrical settings of the x-ray tube, amount, rate and location of contrast agent injection, and delay between injection and acquisition.

The acquisition protocol used in this paper is a tradeoff between clinical, mechanical, and algorithmic constraints encountered in the course of our study. The main clinical constraint is that the whole acquisition has to be performed during a single breath hold to avoid breathing motion. As patients with cardiac or vascular diseases often have reduced breath-holding capabilities,[5] and must start holding their breath before and stop after the acquisition, acquisition itself should not last longer than 10 s. The amount of contrast agent should also be limited, as it adds up to the contrast injected during the intervention. This second constraint also pledges for a short acquisition. On the other hand, because of mechanical constraints, C-arms rotate much slower than CT scanners and cannot perform step and shoot acquisitions.[6] Current C-arms perform a 200° rotation in a minimum of 3–5 s, which implies that a cardiac acquisition always covers several cardiac cycles. Therefore, the projections must be sorted *a posteriori*: each phase of the cardiac cycle is reconstructed using only the projections acquired while the heart was close to this phase, and discarding the others. In tomography with few views, the better the projections cover the angular range around the object, the better is the reconstruction.[7] In cardiac C-arm CT, electrocardiogram gating (ECG gating) results in a few clusters of consecutive projections (one cluster per heart beat), separated by empty angular regions (where other cardiac phases were acquired). To obtain the best possible angular coverage, it is desirable to have as many heart cycles acquired during the C-arm rotation as possible, and thus a long acquisition time. Therefore, the duration of the acquisition must be the result of a tradeoff between the image quality and the safety and comfort of the patient. The 4D reconstruction method presented in this paper targets a cardiac reconstruction from a single sweep 10 s acquisition.

In the last decade, several classes of 4D reconstruction methods have been proposed. Motion compensated reconstructions[8–11] attempt to estimate the motion of the heart, and take it into account in the reconstruction process. They depend on the accuracy of the motion estimation, and as of now have not proven to be efficient on single sweep cardiac C-arm CT data. Methods based on compressed sensing,[12–14] and in particular the prior image constrained compressed sensing method (short PICCS),[7,15] which is the current state of the art in cardiac C-arm CT, compensate the loss of information caused by ECG-gating by introducing sparsity-based regularization priors in the solution. Methods[12–14] attempt to reconstruct each cardiac phase individually, and do not take advantage of the strong similarity between successive car-

diac phases. By imposing that each cardiac phase be close to a single "prior" image, PICCS indirectly enforces similarity between cardiac phases, but this similarity is not stronger between successive phases (e.g., midsystole and end systole) than between distant phases (e.g., end systole and end diastole), which would be a desirable property.

Recently, new algorithms introducing temporal regularization between consecutive cardiac phases have been proposed.[16] The additional constraint introduced by temporal regularization restricts the space of admissible solutions to the temporally consistent ones. As such, it allows the reconstruction algorithm to better exploit the data. A 4D-regularized reconstruction method, based on temporal non-local means (TNLM), was proposed by Jia *et al.*[17] Langet *et al.* have proposed a 3D + time reconstruction algorithm for injected arteries,[18] which is a specific problem leading to specialized algorithms. Momey *et al.* proposed a 2D + time reconstruction method based on total variation (short TV) regularization,[19] and later extended it to 3D + time.[20] In the present paper, we introduce a new 3D + time reconstruction method, which we name 4D ROOSTER (for 4D RecOnstructiOn using Spatial and TEmporal Regularization), by starting from ECG-gated simultaneous algebraic reconstruction technique [SART (Ref. 21)] and adding regularization constraints one by one: first positivity, then restriction of motion to a region of interest (ROI) containing the heart and the vessels, and then spatial and temporal total variation minimization.

It is shown that the proposed method outperforms PICCS both on simulated and real data, and can successfully reconstruct a 3D + time sequence from a 10 s single sweep human cardiac C-arm CT acquisition.

2. MATERIALS AND METHODS

2.A. The 4D ROOSTER method

The 4D ROOSTER method derives from the desired properties of the solution to the problem:

- (P₁) Forward projection through the reconstructed 4D volume should match the measured projection data as accurately as possible.
- (P₂) All voxels should have non-negative attenuation.
- (P₃) No movement should occur outside the heart and the vascular system.
- (P₄) Each volume of the sequence should have some kind of spatial regularity, i.e., be spatially smooth except on the edges of the organs and be free of streak artifacts.
- (P₅) Consecutive volumes in the sequence should be similar.

Before describing the details of the reconstruction method, let us express these requirements in a more formal way. Let $f_1, f_2, \ldots f_N$ be 3D volumes, each one representing a single cardiac phase, and let $f = \begin{pmatrix} f_1 \\ \vdots \\ f_N \end{pmatrix}$ be a 4D volume. Cardiac phases are often expressed in percentage of the cardiac cycle: here the volume f_i represents the cardiac phase $t = (i/N)$. The $f_1, f_2, \ldots f_N$ are column vectors of size M, where M is

the number of voxels in a 3D volume. Thus f is a column vector of size MN. For clarity, the intensity at a voxel (x, y, z) in each volume f_i will also be denoted $f_i(x, y, z)$. p_θ is the real projection measured at angle θ, and R_θ a ray-driven forward projection operator (also called x-ray transform) for angle θ. Note that R_θ is an approximation of the real x-ray transform, and does not take into account scattering, beam hardening, detector cross talk, or gain effects. Corrections for these effects are applied by preprocessing the projections, and the p_θ are in fact the corrected projections. The p_θ are column vectors of size P, where P is the number of pixels in a projection, and the R_θ are matrices with P lines and M columns.

S_θ is an interpolation operator which, from the 3D + time sequence, estimates the 3D volume through which projection θ has been acquired. It is defined as follows: from the ECG, we know in which phase $t(\theta)$ the patient's heart was when projection p_θ was acquired. The forward projection at angle θ, which will be compared to the measured projection p_θ, should be computed through an estimate of the patient's thorax at $t(\theta)$, which by a slight abuse in notation we will denote $f_{t(\theta)}$, and which is obtained by interpolating between some of the volumes f_i. If $N = 10$, f_1 is the volume at 10% of the cardiac cycle, f_2 the volume at 20%, and so on. With $t(\theta) = 87\%$, the interpolated volume would be $S_\theta f = f_{t(\theta)} = 0.3 f_8 + 0.7 f_9$. In this example, and in the implementation we used, S_θ is a linear interpolator. However, other interpolation methods could be tested, like nearest neighbors or splines. Note that S_θ is a huge matrix with M lines and MN columns, but is not explicitly computed in practice.

It is assumed that a ROI of the heart and main vessels is available (for instance, derived from a rough segmentation of the ungated FDK reconstruction), from which the operator H is derived. H is a binary diagonal matrix with M lines, which "selects" those voxels in a volume that are located outside the heart. As a result, for any i,

$$\begin{cases} H f_i(x, y, z) = f_i(x, y, z) \text{ if } (x, y, z) \text{ is outside the heart} \\ \quad H f_i(x, y, z) = 0 \text{ if } (x, y, z) \text{ is inside the heart} \end{cases}.$$
$$(1)$$

Multiplication by the matrix H is the linear algebra equivalent of multiplying by a motion mask. The mask's edges are sharp, which can lead to artifacts at its borders. The spatial regularity constraint seems to be sufficient to mitigate these artifacts in the cases we have studied. Should the need arise, changing to a mask with soft edges would only require slight modifications.

Now, let us formalize our five requirements on the solution:

- (P_1), taken in the least squares sense, means that $\sum_\theta \|(R_\theta S_\theta f - p_\theta)\|_2^2$ should be small.
- (P_2) is equivalent to imposing that $\forall i$ and $\forall (x, y, z)$, $f_i(x, y, z) \geq 0$.
- (P_3) means that for any i and j, $H f_i = H f_j$.
- (P_4) can be enforced by numerous regularization methods. We chose to express it as a constraint on 3D total

variation on each volume f_i. Total variation is defined by

$$\mathrm{TV}_{\mathrm{space}}(f) = \|\sqrt{(\nabla_x f_i)^2 + (\nabla_y f_i)^2 + (\nabla_z f_i)^2}\|_1. \quad (2)$$

The ∇ operator accounts for the spacing between voxels, which can vary from one direction to another.

- (P_5) can also be expressed as a constraint on total variation, although this time a one-dimension total variation has to be used. The following constraint is derived:

$$\mathrm{TV}_{\mathrm{time}}(f) = \|\nabla_t f\|_1 \quad (3)$$

should be small. The discrete gradient along time is computed with a circular boundary condition because the sequence of volumes is meant to be cyclic.

The algorithm we propose in order to derive a 3D + time sequence f that has the aforementioned properties consists in the following steps:

- Start from $k = 0$ and $f^{(k)} = 0$
- Until $k = k_{\max}$

  - Compute $\hat{f} = \underset{f}{\arg\min} \sum_\theta \|(R_\theta S_\theta f - p_\theta)\|_2^2$ by a conjugate gradient descent initialized with $f^{(k)}$
  - Set all negative voxels to zero
  - In each $\hat{f}_i$ replace the area outside the heart by its temporal mean $\frac{1}{N} \sum_j H \hat{f}_j$

  - For each $\hat{f}_i$, compute $\hat{g}_i = \underset{g}{\arg\min} \lambda_{\mathrm{space}} \|g - \hat{f}_i\|_2^2 + \mathrm{TV}_{\mathrm{space}}(g)$ using a gradient descent, as described by Chan,[22] and concatenate the $\hat{g}_i$ into $\hat{g}$

  - Compute $f^{(k+1)} = \underset{f}{\arg\min} \lambda_{\mathrm{time}} \|f - \hat{g}\|_2^2 + \mathrm{TV}_{\mathrm{time}}$ (f) by the same method
- k = k + 1

The parameters of the algorithm are the number of main loop iterations $k_{\max}$ (for all results presented throughout the paper, except those used for Fig. 6, $k_{\max} = 30$), the number of nested conjugate gradient iterations (set to 4 throughout the paper), the number of iterations used in the TV minimization, the parameters λ_{space} and λ_{time}, which are data attachment coefficients for TV minimization, and the steps of the gradient descents.

In order to account for the data truncation when working on real cardiac C-arm CT data, the reconstruction volume was chosen slightly larger than the field of view.[23,24]

In order to demonstrate the impact of each individual regularization step, modified versions of this method have been tested. Each regularization step has been turned off while all others were turned on. The results are presented in Sec. 3.

2.B. The PICCS method

The PICCS method is based on minimizing the following cost function:

$$\mathrm{Cost}(f) = G\|(Rf - p)\|_2^2 + \alpha TV(f - f^*)$$
$$+ (1 - \alpha)TV(f), \quad (4)$$

where f is the 3D volume being reconstructed, f^* is a prior image close to the solution we seek (usually the FDK reconstruction using all projections,[3] also called "ungated FDK"), TV is the total variation operator, R is the x-ray transform operator, p is the set of measured projections, and G is an ECG-gating operator. G is diagonal and, in our case, binary (ECG-gating can be performed with various window shapes,[25] and G is not binary if the chosen shape is not a gate).

There are several ways to estimate a solution f that minimizes this cost function. In this paper, we have implemented a method very close to the one described by Chen *et al.*,[15] in which it was proposed to alternate between iterations of ECG-gated ART,[25,26] to minimize the data attachment term, and steepest descent iterations, to minimize the rest of the cost function, i.e., $(1 - \alpha)\mathrm{TV}(f - f^*) + \alpha\mathrm{TV}(f)$. We used SART (Ref. 21) instead of ART, and turned the cost function minimized by the steepest descent iterations into $\lambda\|f - f_{\mathrm{SART}}\|_2^2 + \alpha\mathrm{TV}(f - f^*) + (1 - \alpha)\mathrm{TV}(f)$, where f_{SART} is the volume returned by the SART step. Adding such a data-attachment term avoids blurring the edges of the reconstructed volume when $\alpha \to 0$.

2.C. Implementation

Both PICCS and 4D ROOSTER have been implemented using the Reconstruction ToolKit (short RTK), a library based on the Insight ToolKit (short ITK).[27] Data truncation was handled the same way in both 4D ROOSTER and PICCS: the reconstruction volume was set larger than the field of view. RTK supports CUDA, thus 4D ROOSTER and PICCS were implemented mostly on GPU. Reconstructions were performed on a 2.8 GHz Intel Xeon with 6 cores, equipped with an nVidia Tesla C2070.

With our implementation of PICCS, it takes about 15 min to reconstruct a single phase, meaning a single $284 \times 216 \times 284$ voxels volume, from about 61 projections (20% of 308 projections) of 512×396 pixels each.

With our implementation of 4D ROOSTER, it takes about 90 min to reconstruct ten phases, meaning a $284 \times 216 \times 284 \times 10$ voxels 3D + time sequence, from 308 projections of 512×396 pixels each.

2.D. Simulations

4D ROOSTER is demonstrated on a 3D Shepp and Logan phantom, in which the size of one of the ellipses varies periodically to simulate a beating heart. The simulated acquisition geometry was chosen close to that of the real acquisition (308 projections regularly distributed over a 205° trajectory, acquired over 10 s, and 60 beats/min). The instant when the beating ellipse is the smallest is called "end systole," and the instant when it is the largest is called "end diastole." The ground truth images for end systole and end diastole are displayed in Fig. 1. The region in which movement is allowed, and in which the local root mean square error (RMSE) is computed (see Table II), is delineated by a circle on the end diastolic image. It has been chosen a little larger than the beating
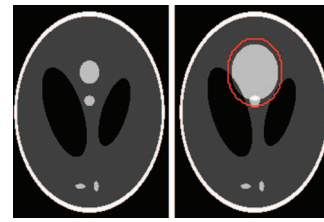

FIG. 1. Ground truth of the Shepp and Logan phantom with a beating ellipse, in end systole (on the left) and end diastole (on the right). The region in which movement is allowed, and in which local RMSE is computed, is delineated by a circle on the end diastolic image.

ellipse in end diastole to illustrate the fact that the segmentation of the heart can be rough and include a margin of error.

2.E. Clinical data

The clinical datasets used in this paper were acquired at the Division of Cardiology, University of Colorado, Denver, USA. The C-arm CT acquisition was performed on an Allura XPer FD20 (Philips Healthcare, Best, The Netherlands). 308 projections were acquired in 10.3 s over a 205° circular arc trajectory, during a single breath hold. Each projection contains 1024×792 pixels of 0.37×0.37 mm (note that for this work the projections have been downsampled by a factor of 2 in both directions). The projections are corrected for detector cross talk, pixel gain, beam hardening, and scatter.[28,29] The tube was set to 83 kV, 650 mA, 10 ms per projection. The CTDI dose delivered to the patient is 4.3 mSv.[30] Patient 1 had a heart rate of 90 beats/min (which is a favorable configuration, see Sec. 1), and patient 2 a heart rate of 60 bpm (which is the target). More details on the acquisition protocol can be found in Schwartz *et al.*[2] Projections 50 and 250 for both patients are displayed in Fig. 2.

As can be observed in projection 50, at its initial concentration, before it gets diluted into blood, the contrast medium has
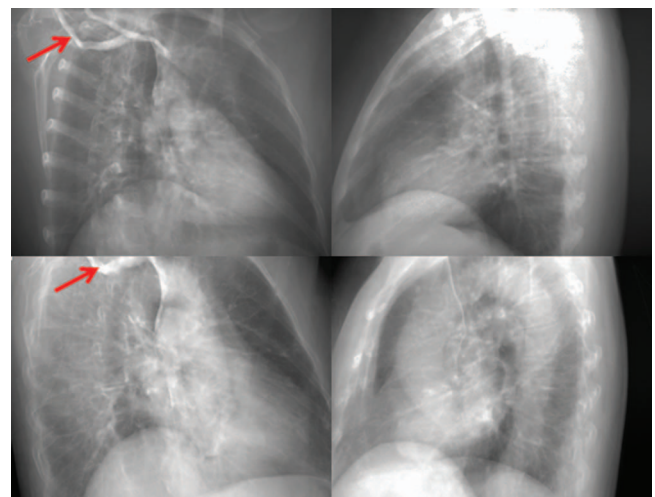

FIG. 2. Projection 50 out of 308 (left column) and 250 out of 308 (right column) of the injected C-arm CT scan performed on patient 1 (top row) and patient 2 (bottom row). The arrows point out the highly concentrated contrast agent in the superior vena cava in projection 50.

a high absorption. This creates hyperattenuation artifacts in the reconstructed volumes, just like metallic objects would do.

Moreover, the contrast medium flows in the vascular system. Its distribution in space can be considered periodic inside the heart if the injection is performed carefully, but is never periodic outside the heart. Therefore, projections acquired at the same ECG-phase can represent different volumes: the flow of the contrast medium makes the projection data inconsistent. Cardiac reconstruction algorithms are nevertheless built on the assumption that the attenuation of a voxel depends only on its position in space and on the ECG-phase considered, or in other words, that the imaged object's attenuation varies periodically like the ECG.

Another source of error is the truncation of data: patients are typically larger than the field of view, so that certain parts of their chest are visible on some projections and not on the others. This also makes the projection dataset inconsistent. In order to mitigate the artifacts caused by truncation, the reconstructed volume has been slightly extended outside the field of view.[24]

2.F. Quantitative evaluation of sharpness

Two methods were used to quantitatively assess the sharpness of the reconstructed clinical data:

- Kriminski's blur criterion,[31] based on the work of Boykov *et al.*,[32, 33] which consists in creating a graph from the image, performing a graph cut segmentation, and using the maximum flow (or equivalently the minimal cut weight) as a measure of blur, as performed in Rit *et al.*[23]
- Contrast to noise ratio (CNR).

Kriminski's method provides a measure of blur derived from a graph cut segmentation. It makes particular sense in our case to introduce a segmentation-based criterion since one of the main goals of the cardiac reconstruction we are targeting is to segment the blood in the left ventricle, e.g., to compute the left ventricular ejection fraction. Kriminski's blur criterion requires only one parameter, which can roughly be interpreted as an intensity threshold and was tuned manually for each reconstructed image in order to obtain the best possible segmentation.

CNR does not exactly measure sharpness, but it gives an indication of how distinguishable from one another two adjacent regions are. It was computed as

$$\text{CNR} = \frac{|M_{\text{blood}} - M_{\text{muscle}}|}{\sigma_{\text{muscle}}}, \qquad (5)$$

where M_{blood} and M_{muscle} are the mean attenuations in the blood and muscle ROIs, respectively, and σ_{muscle} is the standard deviation in the muscle ROI.

Figure 3 shows the subimage used for the max flow measurement, and the ROIs used for the CNR measurement, on both patients.
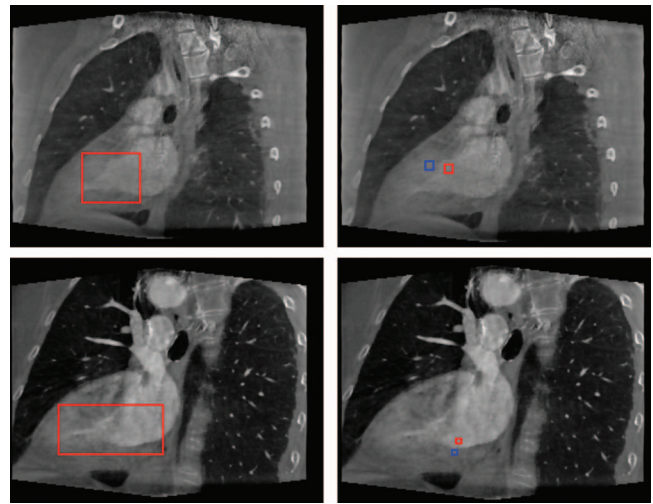

FIG. 3. Region of the image in which the Kriminski blur criterion was measured (left column) and ROIs for the CNR computation (right column) on both patient 1 (top row) and patient 2 (bottom row). Measurements were performed on the long axis cut in systole.

3. RESULTS

3.A. Simulations on a modified Shepp and Logan phantom: From ECG-gated SART to 4D ROOSTER

The 4D ROOSTER method is introduced here by going back to ECG-gated SART, and modifying it step by step to obtain 4D ROOSTER. Reconstructions of the modified Shepp and Logan phantom are shown in Figs. 4 and 5, and the reconstruction parameters for ECG-gated SART and 4D ROOSTER are listed in Table I.

In Fig. 4, all reconstructions are initialized with a zero volume. In Fig. 5, the algorithms are initialized with the ungated FDK reconstruction. In both figures, the top line contains the reconstructions of the systolic phase, the bottom lines the reconstructions of the diastolic phase. From left to right, the algorithms used are the following:

- ECG-gated SART;
- 4D reconstruction by conjugate gradient without any regularization (P_1);
- 4D reconstruction by conjugate gradient alternated with positivity enforcement ($P_1 + P_2$);
- 4D reconstruction by conjugate gradient, alternated with positivity enforcement and averaging along time outside the heart ($P_1 + P_2 + P_3$);
- 4D reconstruction by conjugate gradient, alternated with positivity enforcement, averaging along time outside the heart and minimization of spatial TV ($P_1 + P_2 + P_3 + P_4$);
- 4D ROOSTER as described in Sec. 2.A ($P_1 + P_2 + P_3 + P_4 + P_5$).

Figures 4 and 5 both show that each regularization step brings some improvement, either by reducing the impact of artifacts, sharpening the borders of the beating ellipse or enforcing smoothness in homogeneous regions. The comparison
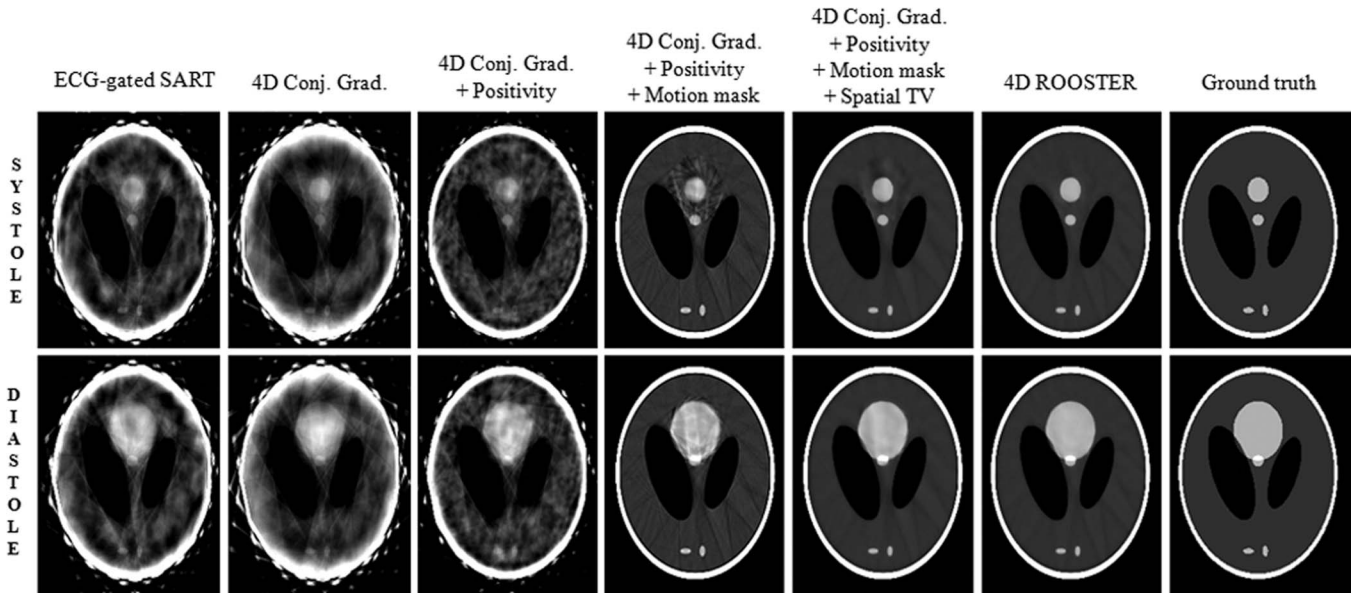
FIG. 4. From ECG-gated SART (first column) to 4D ROOSTER (last column) when initializing with zero. The second column shows the results of unregularized 4D reconstruction by conjugate gradient. The positivity constraint is added in the third column, the motion mask in the fourth column. In the fifth column, spatial regularization by TV minimization is enforced. In the last column, temporal regularization by TV minimization is added to obtain the 4D ROOSTER method. The display window is [0.15; 0.35].

between Figures 4 and 5 also reveals that ECG-gated SART is much more dependent on initialization than 4D ROOSTER is.

A numerical evaluation of the results presented in Figs. 4 and 5 was performed. The parameters retained are the RMSE with respect to the 4D phantom in the whole 4D sequence, and the RMSE in the region where movement can occur (local RMSE) for the 4D phantom. These values are shown in Table II and confirm the gradual improvement brought by

adding each regularization step, which can be appreciated by visual evaluation of Figs. 4 and 5.

Table II shows a reduction of the RMSE and the RMSE in the motion mask when the various regularization steps are added.

Figure 6 shows the evolution of RMSE during the 4D ROOSTER reconstructions of the moving Shepp and Logan phantom. It constitutes a numerical validation of the
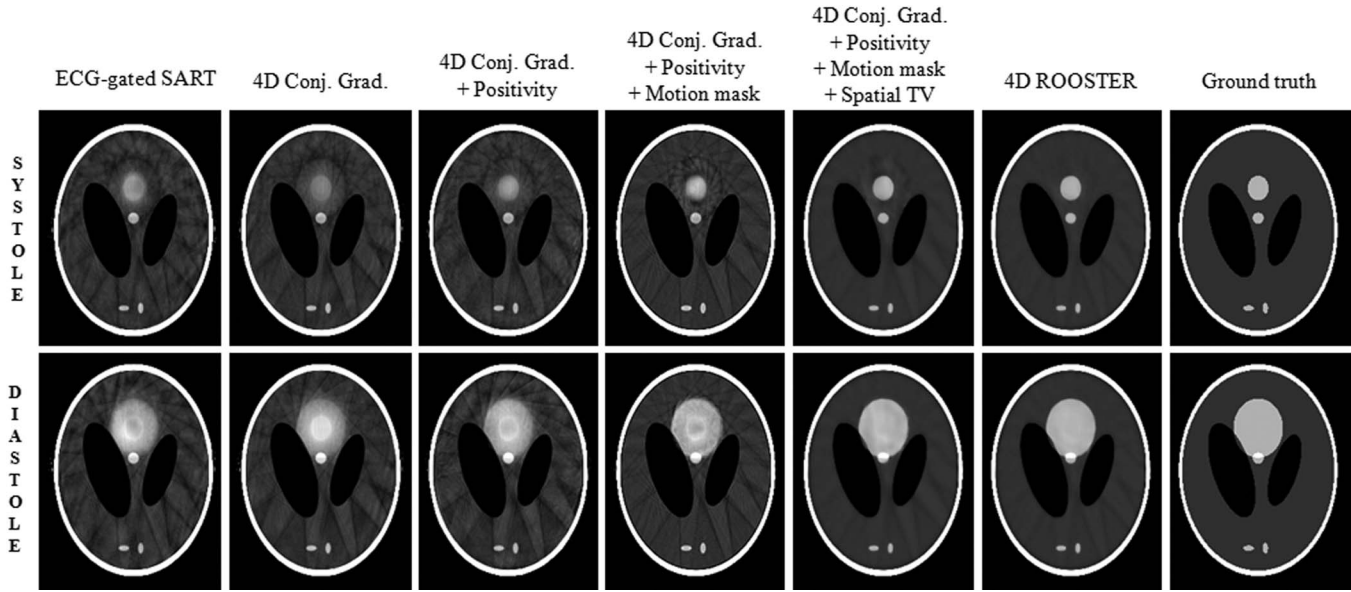

FIG. 5. From ECG-gated SART (first column) to 4D ROOSTER (last column) when initializing with the ungated FDK reconstruction. The second column shows the results of unregularized 4D reconstruction by conjugate gradient. The positivity constraint is added in the third column, the motion mask in the fourth column. In the fifth column, spatial regularization by TV minimization is enforced. In the last column, temporal regularization by TV minimization is added to obtain the 4D ROOSTER method. The display window is [0.15; 0.35].

TABLE I. Parameters used for the reconstructions of the beating Shepp and Logan with ECG-gated SART and 4D ROOSTER.

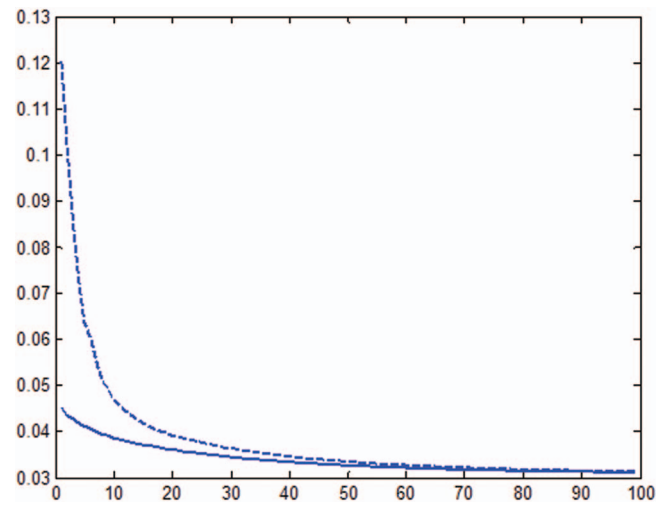| Parameter	SART	4D ROOSTER
Size (in voxels)	$256 \times 256 \times 256$	$256 \times 256 \times 256$
Voxel spacing (in mm)	$1 \times 1 \times 1$	$1 \times 1 \times 1$
Main loop iterations	100	30
SART-specific parameters		
SART relaxation parameter	0.5	
Gating window width (% of cardiac cycle)	20	
4D ROOSTER-specific parameters		
lambda_space		100
lambda_time		100
Nested iterations for spatial TV		5
Nested iterations for temporal TV		5
Gradient descent step for spatial TV		0.001
Gradient descent step for temporal TV		0.001

FIG. 6. Evolution of the RMSE plotted against the number of iterations during the reconstruction of the moving Shepp and Logan phantom. The solid line is the reconstruction initialized with the ungated FDK and the dotted line is the reconstruction initialized with zero.

convergence of 4D ROOSTER, for which we give no formal proof in this paper. More details on convergence can be found in Sec. 4.B. It also highlights the benefit of initializing 4D ROOSTER with the ungated FDK image. In the rest of the paper, 4D ROOSTER has been configured to perform 30 iterations, which in practice seems sufficient, and to start from the ungated FDK reconstruction.

We present in Fig. 7 the absolute value of the difference between the first and second instants of the cardiac cycle (10% and 20% of the cardiac cycle, respectively) for the ECG-gated SART (on the left) and 4D ROOSTER (on the right) reconstructions initialized with ungated FDK. We have zoomed on the region where movement occurs (the ROI is delineated by a circle in Fig. 7). The slice considered is the same as in Figs. 4 and 5. Both the background and the inside of the ROI appear corrupted by temporally moving artifacts in the case of ECG-gated SART, while no such artifacts are present in the background and very little in the ROI on 4D ROOSTER results. It can also be observed that the ring corresponding to the beating ellipse is sharper and more contrasted on the 4D ROOSTER result.
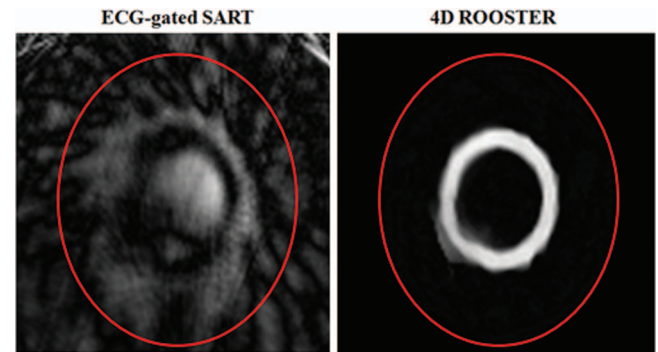

FIG. 7. Absolute value of the difference between the first and second instants of the cardiac cycle, extracted from the ECG-gated SART (left) and 4D ROOSTER (right) reconstructions initialized with ungated FDK. The figure is a zoom on the region where movement occurs, delineated by a circle. These images were computed on the same spatial slice as the one displayed in Fig. 4. The display window is [0; 0.1].

3.B. Clinical results: Comparison with ECG-gated SART and PICCS

In this section, reconstruction results obtained with ECG-gated SART, PICCS, and 4D ROOSTER on two clinical cases are presented. The results were not converted to Hounsfield

TABLE II. Root mean square error ECG-gated SART, 4D ROOSTER, and all intermediate reconstruction methods with partial regularization.

	Initialization: zero		Initialization: ungated FDK	
	RMSE	RMSE in ROI	RMSE	RMSE in ROI
ECG-gated SART	0.0954	0.0319	0.0472	0.0278
4D CG	0.1134	0.0345	0.0474	0.0245
4D CG + positivity	0.0698	0.0247	0.0425	0.0211
4D CG + positivity + motion mask	0.0387	0.0168	0.0379	0.0182
4D CG + positivity + motion mask + spatial TV	0.0365	0.0122	0.0345	0.0122
4D ROOSTER	0.0363	0.0113	0.0345	0.0113

TABLE III. Parameters used for the reconstructions of the clinical case with ECG-gated SART, PICCS, and 4D ROOSTER.

Parameter	SART	PICCS	4D ROOSTER
Size (in voxels)	$284 \times 216 \times 284$	$284 \times 216 \times 284$	$284 \times 216 \times 284$
Voxel spacing (in mm)	$1 \times 1 \times 1$	$1 \times 1 \times 1$	$1 \times 1 \times 1$
Main loop iterations	100	30	30
SART-specific parameters			
SART relaxation parameter	0.5		
Gating window width (% of cardiac cycle)	20		
PICCS-specific parameters			
Alpha		0.5	
Lambda		500	
SART relaxation parameter		0.5	
Nested gradient descent iterations		20	
Gradient descent step		0.002	
Gating window width (% of cardiac cycle)		20	
4D ROOSTER-specific parameters			
lambda_space			10000
lambda_time			1000
Nested iterations for spatial TV			10
Nested iterations for temporal TV			10
Gradient descent step for spatial TV			0.0002
Gradient descent step for temporal TV			0.0002

units: attenuations are expressed in mm^{-1}. The parameters used for the reconstructions of this section are listed in Table III.

Figure 8 shows reconstructions of the end systolic and end diastolic phases of the first patient's heart, on a long axis cut of the left ventricle.

Figure 9 shows the reconstructions of the end systolic and end diastolic phases of the first patient's heart, on a short axis cut. In both Figs. 8 and 9, the 4D ROOSTER results are sharper than the PICCS ones, and far less noisy than the ECG-gated SART results. The border between the endocardium and the interior of the left ventricle, pointed out by an arrow, is easy to identify on the 4D ROOSTER results while it is hard to determine with precision on the PICCS or SART results.

In the PICCS reconstructions, some streak artifacts remain and cause variations of the attenuation in regions that should be static. They can be observed in Fig. 8, in the top left corner of the PICCS reconstructions, which differ a lot while they should not. However, our main objective is to obtain a good reconstruction inside the heart region. From this standpoint, Figure 10 is more relevant. It shows the difference between two consecutive cardiac phases for both PICCS and 4D ROOSTER, and highlights the temporal consistency of 4D ROOSTER reconstructions both outside and inside the heart.

Figures 11 and 12 show the reconstructions of the second patient, in long axis cut for Fig. 11 and in short axis cut for Fig. 12. Because patient 2 has a lower heart rhythm than patient 1, the undersampling problem is more acute, and the reconstructed images are less sharp. The arrow in Fig. 11 points a portion of the border between blood and myocardium where sharpness differs a lot between SART, PICCS, and ROOSTER results.

A quantitative evaluation of sharpness using the methods described in Sec. 2.F is presented in Table IV. SART reconstructions are noisier and blurrier than PICCS images, which in turn are noisier and blurrier than 4D ROOSTER reconstructions.
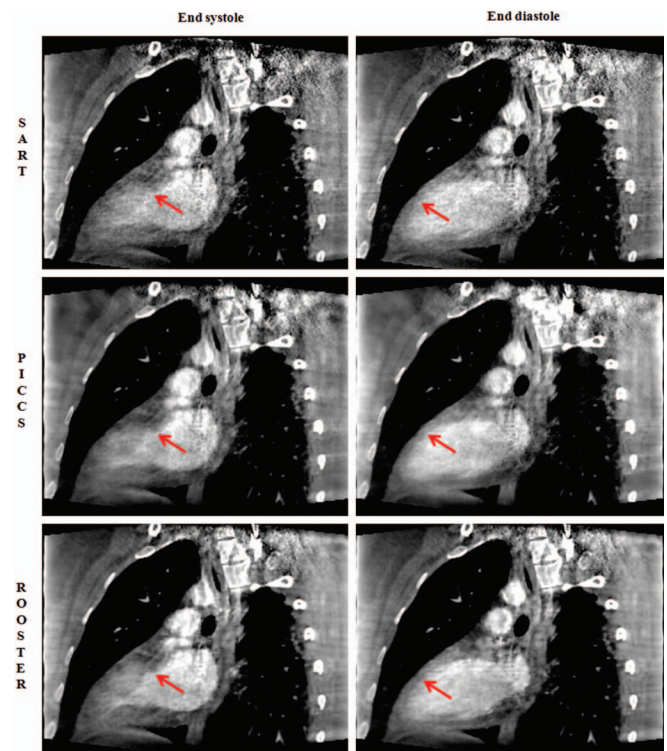

FIG. 8. Long axis cuts of the left ventricle in ECG-gated SART, PICCS, and 4D ROOSTER reconstructions of patient 1. The display window is [0.018; 0.042].
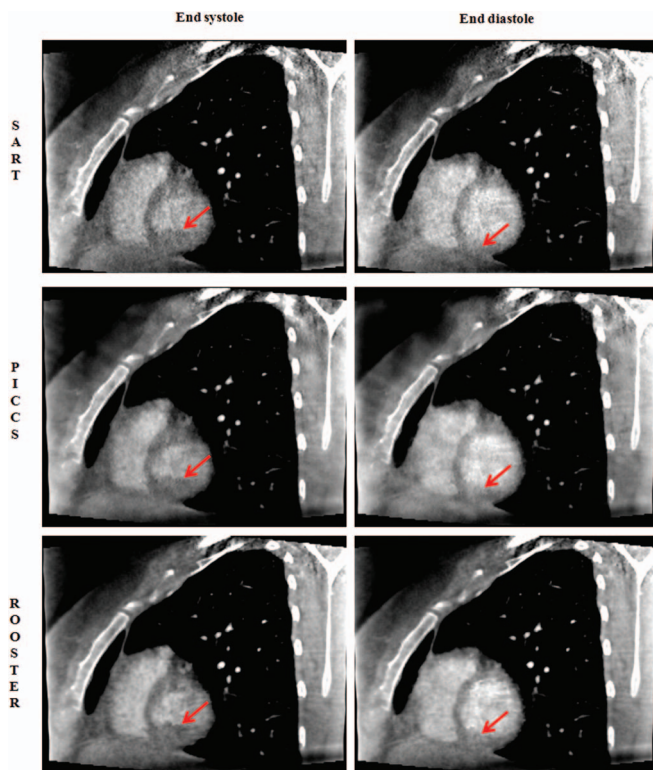
FIG. 9. Short axis cuts of the left ventricle in ECG-gated SART, PICCS, and 4D ROOSTER reconstructions of patient 1. The display window is [0.018; 0.042].
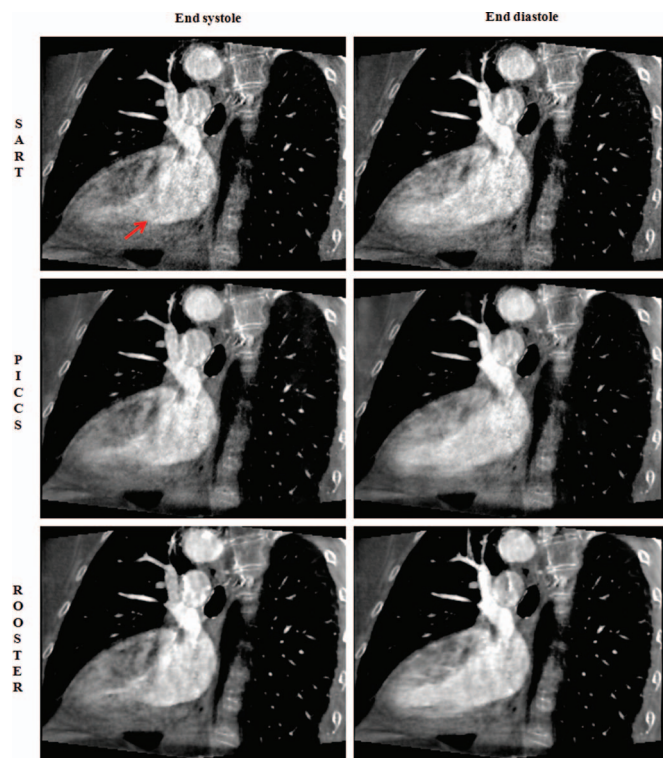

FIG. 11. Long axis cuts of the left ventricle in ECG-gated SART, PICCS, and 4D ROOSTER reconstructions of patient 2. The display window is [0.01; 0.042].

3.C. Impact of each regularization step

Understanding the practical impact of each regularization step on the final result is crucial to be able to fine-tune the parameters of the 4D ROOSTER algorithm. This section presents the results obtained with 4D ROOSTER on the clinical dataset when all regularization steps but one are active, so as to give some insight on the role of each step. Figure 13 shows that positivity enforcement has little impact in this case. However, it does not deteriorate the image, comes at a very small computational cost (see Table V), and as it can be seen in Fig. 4, it plays an important role when initializing with zero. Therefore, we recommend keeping this regularization step.
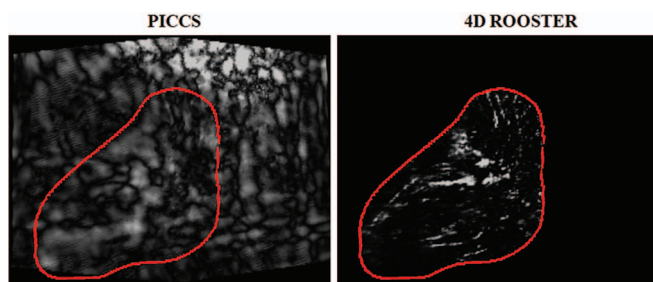

FIG. 10. Absolute value of the difference between two consecutive cardiac phases in both PICCS and 4D ROOSTER, in the same long axis cut as in Fig. 8. The contour is the border of the ROI used in 4D ROOSTER. The display window is [0; 0.005].

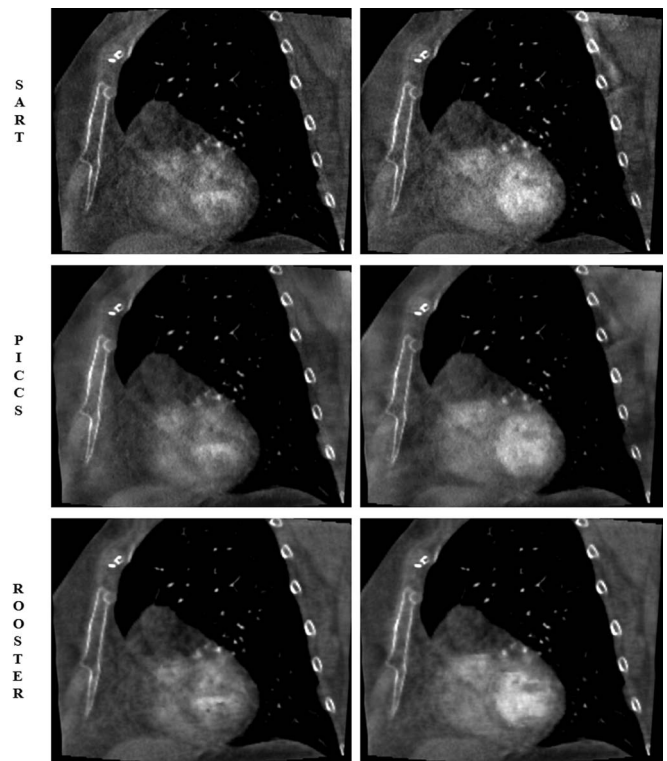FIG. 12. Short axis cuts of the left ventricle in ECG-gated SART, PICCS and 4D ROOSTER reconstructions of patient 2. The display window is [0.01; 0.042].

TABLE IV. Quantitative evaluation of sharpness in reconstructions of clinical cases.

	SART	PICCS	ROOSTER
Patient 1			
Blur criterion	13.7	10.8	7.8
CNR	1.33	3.3	4.47
Patient 2			
Blur criterion	11.3	10.2	9.7
CNR	6.09	6.39	11.98

TABLE V. Computation time required for each step of the 4D ROOSTER method.

Algorithm step	Computation time (s)
Conjugate gradient minimization of data attachment	110
Positivity enforcement	0.1
Temporal averaging outside heart ROI	14
Spatial TV minimization	14
Temporal TV minimization	30

The effect of spatial regularization is shown in Fig. 14. Minimizing the 3D total variation effectively removes high frequency noise and favors solutions with homogeneous regions separated by sharp edges.

Figure 15 highlights the role averaging along time outside the motion mask and of minimizing temporal TV by displaying the difference image between two consecutive heart phases. Minimizing temporal TV seems to have a higher impact on image quality than averaging outside the motion mask, but both regularization steps appear complementary.

4. DISCUSSION AND CONCLUSION

4.A. Comparison with PICCS

The 4D ROOSTER method has been introduced and compared to PICCS on real human cardiac C-arm CT data. As PICCS is designed to reconstruct textured data, we have chosen not to present comparisons between PICCS and 4D ROOSTER on the moving Shepp and Logan phantom, which would have been unfair to PICCS and irrelevant. The results obtained on real data confirm the superiority of 4D ROOSTER over PICCS. The main reasons why 4D ROOSTER achieves better results than PICCS are the following:

- It uses a motion mask to allow movement only where it is supposed to occur. This is a strong hypothesis, which considerably reduces the number of unknowns of the reconstruction problem.
- It uses regularization along time, which rules out many inconsistent solutions, and is also highly efficient in removing streak artifacts.
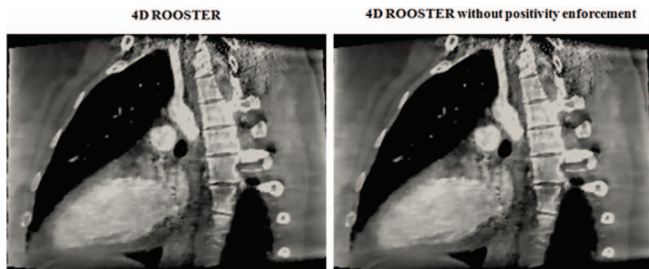
A clinical study with more patients, and in particular patients with lower heart rates, is necessary to confirm the results of this comparison.

It could be argued that, with different parameters, it would have been possible to obtain better images using PICCS (potentially better than using 4D ROOSTER). There are indeed many parameters in both methods, and we cannot guarantee that the ones we chose are the best. For each method, the results presented in the paper are the best ones we were able to obtain, and the parameters used to obtain them are listed in Tables I and III.

4.B. Convergence of the 4D ROOSTER method

Unlike a large class of reconstruction methods based on compressed sensing,[7,14,20,34] 4D ROOSTER does not consist in minimizing a cost function defined as the sum of a data-attachment term and one or more regularization terms. Instead, it alternates between several optimization goals. Similar methods include the adaptive steepest descent-projection onto convex sets (ASD-POCS) (Ref. 13) and some PICCS implementations, like the one we used. The proof of convergence for such an alternating algorithm is typically harder than for a method minimizing a single cost function.

This section provides the theoretical background to prove that if the algorithm has at least one fixed point, it converges to one of its fixed points. We do not prove here that such a fixed point does exist. Using the same notations as in Sec. 2.A, a few definitions from the theory of nonexpansive mappings are reminded:

- A mapping T: $\mathbb{R}^{MN} \to \mathbb{R}^{MN}$ is nonexpansive if $\forall x, y \in \mathbb{R}^{MN}$, $\|Tx - Ty\|_2 \leq \|x - y\|_2$.

FIG. 13. Comparison between 4D ROOSTER and 4D ROOSTER without positivity enforcement [i.e., removing property (P$_2$)]. The display window is [0.017; 0.04].
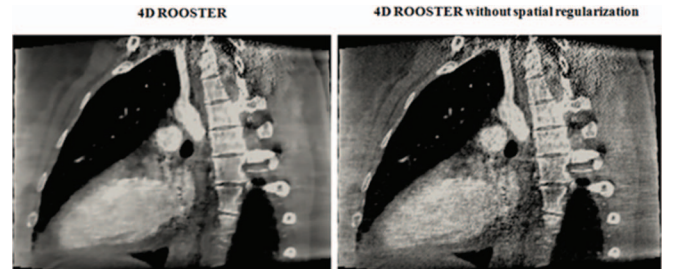

FIG. 14. Comparison between 4D ROOSTER and 4D ROOSTER without spatial regularization [i.e., removing property (P$_4$)]. The display window is [0.017; 0.04].
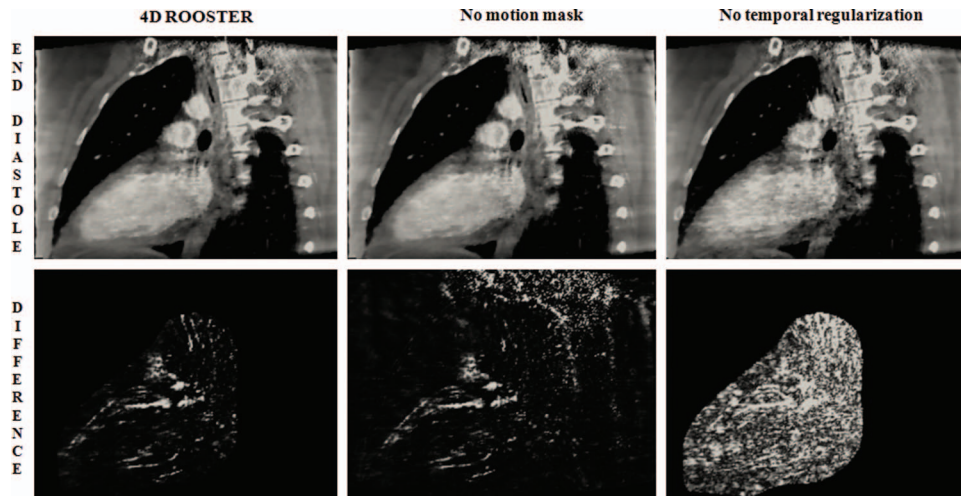
FIG. 15. Comparison between 4D ROOSTER in the left column, 4D ROOSTER without motion mask [i.e., removing property (P$_3$)] in the middle column and 4D ROOSTER without temporal regularization [i.e., removing property (P$_5$)] in the right column. The top row shows the end-diastolic phase and the bottom row shows the absolute value of the difference between two consecutive cardiac phases. Even in large homogeneous areas where the attenuation should not change much over time, like inside the left ventricle near the base, important differences are noticeable between successive phases if temporal regularization is not applied. Averaging outside the motion mask also removes some of the high frequency noise. The display window is [0.017; 0.04] for the top row and [0; 0.005] for the bottom row.

- T is strongly nonexpansive if T is nonexpansive and whenever $(x_n)_{n \in \mathbb{N}}$ and $(y_n)_{n \in \mathbb{N}}$ are sequences in $\mathbb{R}^{MN}$ such that $(x_n - y_n)_{n \in \mathbb{N}}$ is bounded and $\|x_n - y_n\|_2 - \|Tx_n - Ty_n\|_2 \to 0$, it follows that $(x_n - y_n) - (Tx_n - Ty_n) \to 0$.
- T is firmly nonexpansive if $\forall x, y \in \mathbb{R}^{MN}$, $\|Tx - Ty\|_2^2 \leq \langle Tx - Ty, x - y \rangle$.

All operators involved in 4D ROOSTER are strongly nonexpansive:

- In our problem, with enough iterations, conjugate gradient descent is strongly nonexpansive.
- Positivity enforcement is a projector onto a nonempty closed convex set, therefore it is firmly nonexpansive, and therefore strongly nonexpansive (see fact 4.2 of Bauschke *et al.*[35]).
- It is easy to prove that averaging along time outside the motion mask is a firmly nonexpansive mapping.
- The spatial and temporal TV regularization operators are proximal mappings, therefore they are firmly nonexpansive,[36] and therefore strongly nonexpansive.

As stated in fact 4.2 of Bauschke *et al.*,[35] the composition of a finite number of strongly nonexpansive mappings is a strongly nonexpansive mapping. Thus, each iteration of the main loop of 4D ROOSTER amounts to applying a strongly nonexpansive mapping T on the current 3D + time sequence f_k, such that $f_{k+1} = T(f_k)$. Applying the theorem reminded in fact 4.3 of Bauschke *et al.*,[35] if T has at least one fixed point, 4D ROOSTER converges to one of its fixed points.

4.C. Segmentation of the heart and vessels

The constraint that the sequence be static outside the heart and vessels reduces the number of unknowns by an order of magnitude, but assumes that a segmentation of the heart and vessels is available. For this paper the segmentation has been performed on the ungated FDK reconstruction using the semiautomatic segmentation tool LiveMorph.[37] It could be replaced by a fully automatic method,[2] especially because the segmentation used by 4D ROOSTER can be very rough, and can handle small segmentation errors.

4.D. Perspectives

Future work on the method includes the study of regularization methods other than total variation minimization, potentially better suited to textured data (e.g., wavelets, curvelets, nonlocal means, etc.). For the clinical part, 4D ROOSTER could be tested on—and maybe adapted to—specific applications like late enhancement cardiac C-arm CT for myocardial infarction imaging or cardiac imaging in children with congenital heart defect.

4.E. Conclusion

4D ROOSTER can be applied for single sweep human cardiac C-arm CT, and potentially other dynamic tomography areas. It can easily be adapted by modifying the regularization constraints, as regularization is decoupled from projection and back projection.

ACKNOWLEDGMENT

a)Author to whom correspondence should be addressed. Electronic mail: cyril.mory@philips.com; Telephone: +33472357412.

[1] A. Thiagalingam *et al.*, "Intraprocedural volume imaging of the left atrium and pulmonary veins with rotational x-ray angiography: Implications for catheter ablation of atrial fibrillation," J. Cardiovasc. Electrophysiol. **19**(3), 293–300 (2008).

[2]J. G. Schwartz, A. M. Neubauer, T. E. Fagan, N. J. Noordhoek, M. Grass, and J. D. Carroll, "Potential role of three-dimensional rotational angiography and C-arm CT for valvular repair and implantation," Int. J. Cardiovasc. Imaging **27**(8), 1205–1222 (2011).

[3]L. A. Feldkamp, L. C. Davis, and J. W. Kress, "Practical cone-beam algorithm," J. Opt. Soc. Am. A **1**(6), 612–619 (1984).

[4]U. D. Numburi, S. R. Kapadia, P. Schoenhagen, E. M. Tuzcu, M. Roden, and S. S. Halliburton, "Optimization of acquisition and contrast injection protocol for C-arm CT imaging in transcatheter aortic valve implantation: Initial experience in a swine model," Int. J. Cardiovasc. Imaging **29**(2), 405–415 (2012).

[5]S. B. Gay, C. L. Sistrom, C. A. Holder, and P. M. Suratt, "Breath-holding capability of adults. Implications for spiral computed tomography, fast-acquisition magnetic resonance imaging, and angiography," Invest. Radiol. **29**(9), 848–851 (1994).

[6]J. Hsieh, J. Londt, M. Vass, J. Li, X. Tang, and D. Okerlund, "Step-and-shoot data acquisition and reconstruction for cardiac x-ray computed tomography," Med. Phys. **33**(11), 4236–4248 (2006).

[7]G.-H. Chen *et al.*, "Time-resolved interventional cardiac C-arm cone-beam CT: An application of the PICCS algorithm," IEEE Trans. Med. Imaging **31**(4), 907–923 (2012).

[8]U. van Stevendaal, J. von Berg, C. Lorenz, and M. Grass, "A motion-compensated scheme for helical cone-beam reconstruction in cardiac CT angiography," Med. Phys. **35**(7), 3239–3251 (2008).

[9]M. Prümmer, J. Hornegger, G. Lauritsch, L. Wigström, E. Girard-Hughes, and R. Fahrig, "Cardiac C-arm CT: A unified framework for motion estimation and dynamic CT," IEEE Trans. Med. Imaging **28**(11), 1836–1849 (2009).

[10]C. Rohkohl, G. Lauritsch, L. Biller, M. Prümmer, J. Boese, and J. Hornegger, "Interventional 4D motion estimation and reconstruction of cardiac vasculature without motion periodicity assumption," Med. Image Anal. **14**(5), 687–694 (2010).

[11]A. A. Isola, A. Ziegler, D. Schäfer, T. Köhler, W. J. Niessen, and M. Grass, "Motion compensated iterative reconstruction of a region of interest in cardiac cone-beam CT," Comput. Med. Imaging Graph. **34**(2), 149–159 (2010).

[12]J. Song, Q. H. Liu, G. A. Johnson, and C. T. Badea, "Sparseness prior based iterative image reconstruction for retrospectively gated cardiac micro-CT," Med. Phys. **34**(11), 4476–4483 (2007).

[13]E. Y. Sidky and X. Pan, "Image reconstruction in circular cone-beam computed tomography by constrained, total-variation minimization," Phys. Med. Biol. **53**(17), 4777–4807 (2008).

[14]C. Mory *et al.*, "ECG-gated C-arm computed tomography using L1 regularization," in *2012 Proceedings of the 20th European Signal Processing Conference (EUSIPCO)* (Bucharest, Romania, 2012), pp. 2728–2732.

[15]G.-H. Chen, J. Tang, and S. Leng, "Prior image constrained compressed sensing (PICCS)," Proc. Soc. Photo Opt. Instrum. Eng. **6856**, 685618 (2008).

[16]E. Hansis, H. Schomberg, K. Erhard, O. Dössel, and M. Grass, "Four-dimensional cardiac reconstruction from rotational x-ray sequences: First results for 4D coronary angiography," Proc. SPIE **7258**, 72580B-1–72580B-11 (2009).

[17]X. Jia, Y. Lou, B. Dong, Z. Tian, and S. Jiang, "4D computed tomography reconstruction from few-projection data via temporal non-local regularization," in *Medical Image Computing and Computer-Assisted Intervention (MICCAI 2010)*, edited by T. Jiang, N. Navab, J. P. W. Pluim, and M. A. Viergever (Springer, Berlin, 2010), pp. 143–150.

[18]H. Langet *et al.*, "Compressed sensing dynamic reconstruction in rotational angiography," Med. Image Comput. Comput. Assist. Interv. **15**(Pt 1), 223–230 (2012).

[19]F. Momey, L. Denis, C. Mennessier, É. Thiébaut, J.-M. Becker, and L. Desbat, "A B-spline based and computationally performant projector for iterative reconstruction in tomography—Application to dynamic X-ray gated CT," in *2012 Second International Conference on Image Formation in X-Ray Computed Tomography*, 2012.

[20]F. Momey, *Reconstruction en Tomographie Dynamique par Approche Inverse Sans Compensation de Mouvement* (Université Jean Monnet, Saint-Etienne, 2013).

[21]A. H. Andersen and A. C. Kak, "Simultaneous algebraic reconstruction technique (SART): A superior implementation of the art algorithm," Ultrason. Imaging **6**(1), 81–94 (1984).

[22]T. F. Chan, S. Osher, and J. Shen, "The digital TV filter and nonlinear denoising," IEEE Trans. Image Process. **10**(2), 231–241 (2001).

[23]S. Rit, D. Sarrut, and L. Desbat, "Comparison of analytic and algebraic methods for motion-compensated cone-beam CT reconstruction of the thorax," IEEE Trans. Med. Imaging **28**(10), 1513–1525 (2009).

[24]B. Zhang and G. L. Zeng, "Two-dimensional iterative region-of-interest (ROI) reconstruction from truncated projection data," Med. Phys. **34**(3), 935–944 (2007).

[25]T. Nielsen, R. Manzke, R. Proksa, and M. Grass, "Cardiac cone-beam CT volume reconstruction using ART," Med. Phys. **32**(4), 851–860 (2005).

[26]R. Gordon, R. Bender, and G. T. Herman, "Algebraic reconstruction techniques (ART) for three-dimensional electron microscopy and X-ray photography," J. Theor. Biol. **29**(3), 471–481 (1970).

[27]S. Rit, M. Vila Oliva, S. Broumische, R. Labarbe, D. Sarrut, and G. C. Sharp, "The reconstruction toolkit (RTK), an open-source cone-beam CT reconstruction toolkit based on the insight toolkit (ITK)," in *International Conference on the Use of Computers in Radiation Therapy (ICCR)*, Melbourne, Australia, 2013.

[28]M. Bertram, J. Wiegert, and G. Rose, "Scatter correction for cone-beam computed tomography using simulated object models," Proc. SPIE **6142**, 61421C-1–61421C-12 (2006).

[29]M. Bertram, S. Hohmann, and J. Wiegert, "Scatter correction for flat detector cone-beam CT based on simulated sphere models," Med. Phys. **34**, 2342–2343 (2007).

[30]D. Schäfer, M. Ahrens, P. Eshuis, and M. Grass, "Low kV rotational 3D x-ray imaging for improved CNR of iodine contrast agent," Proc. SPIE **8313**, 83132V-1–83132V-6 (2012).

[31]S. Kriminski *et al.*, "Respiratory correlated cone-beam computed tomography on an isocentric C-arm," Phys. Med. Biol. **50**(22), 5263–5280 (2005).

[32]Y. Boykov, O. Veksler, and R. Zabih, "Fast approximate energy minimization via graph cuts," IEEE Trans. Pattern Anal. Mach. Intell. **23**(11), 1222–1239 (2001).

[33]Y. Y. Boykov and M.-P. Jolly, "Interactive graph cuts for optimal boundary and region segmentation of objects in ND images," in *Proceedings of Eighth IEEE International Conference on Computer Vision, 2001 (ICCV 2001)* (Vancouver, British Columbia, Canada, 2001), pp. 105–112.

[34]I. Daubechies, M. Defrise, and C. De Mol, "An iterative thresholding algorithm for linear inverse problems with a sparsity constraint," Commun. Pure Appl. Math. **57**(11), 1413–1457 (2004).

[35]H. H. Bauschke, V. Martín-Márquez, S. M. Moffat, and X. Wang, "Compositions and convex combinations of asymptotically regular firmly non-expansive mappings are also asymptotically regular," Fixed Point Theory Appl. **2012**(1), 53 (2012).

[36]H. H. Bauschke and P. L. Combettes, "The Baillon-Haddad theorem revisited," preprint arXiv:0906.0807 (2009).

[37]B. Mory, O. Somphone, R. Prevost, and R. Ardon, "Real-Time 3d image segmentation by user-constrained template deformation," in *Medical Image Computing and Computer-Assisted Intervention—MICCAI 2012* (Springer, Nice, France, 2012), pp. 561–568.